Supplement of Biogeosciences, 23, 8507–8536, 2026
https://doi.org/10.5194/bg-23-8507-2026-supplement
© Author(s) 2026. CC BY 4.0 License.



Biogeosciences Open Access EGU

Supplement of

Evaluating GNSS-T VOD sensitivity to plant water dynamics, rainfall interception, and dew in a coniferous forest

Konstantin Schellenberg et al.

Correspondence to: Konstantin Schellenberg (konstantin.schellenberg@uni-jena.de)

The copyright of individual parts of the supplement might differ from the article licence.

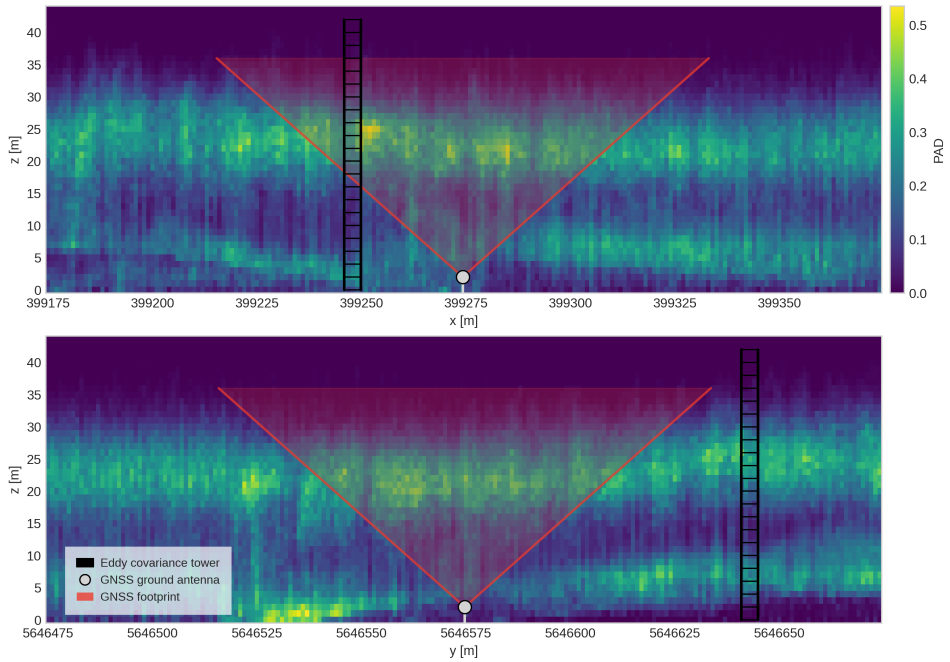


Figure S1: Vertical cross-sections through the GNSS-T ground receiver footprint, along the x–z (top) and the y–z plane (bottom). The terrestrial laser scanning-based plant area density (PAD, $m^2\ m^{-3}$) is shown in the background to illustrate the biomass distribution at the Tharandt research site. Undergrowth is partly found in the footprint but is not abundant in the footprint itself. The eddy covariance tower is depicted in black and does not overlap with the footprint. The canopy height is calculated as the height at which 99.9% of the PAD is reached. The cutoff incidence angle for GNSS-T VOD calculations is 60°.

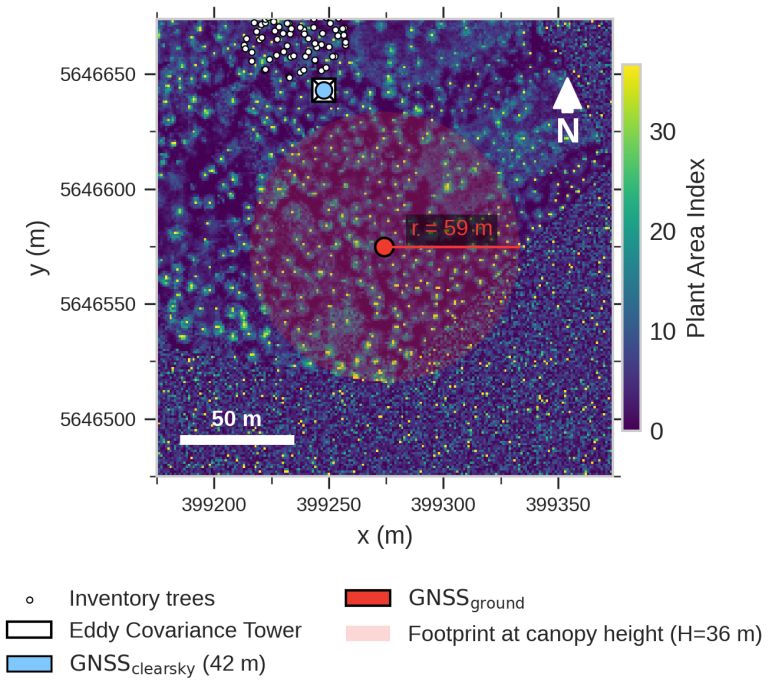


Figure S2: Top-down view (x–y plane) of the GNSS-T ground receiver footprint at the Tharandt research site. The background shows the plant area index ($m^2\ m^{-2}$), i.e. the plant area density of Fig. S1 summed over the z-dimension. The shaded circle marks the footprint at canopy height (H = 36 m), corresponding to a radius of 59 m around the ground antenna. Also shown are the inventory trees, the eddy covariance tower, and the clear-sky reference antenna mounted at 42 m. There was missing lidar data in the most Southern part of the area which overlap with the GNSS cone subset by very little. To avoid missing data in the models, we randomly extrapolated full-column distribution into that area.

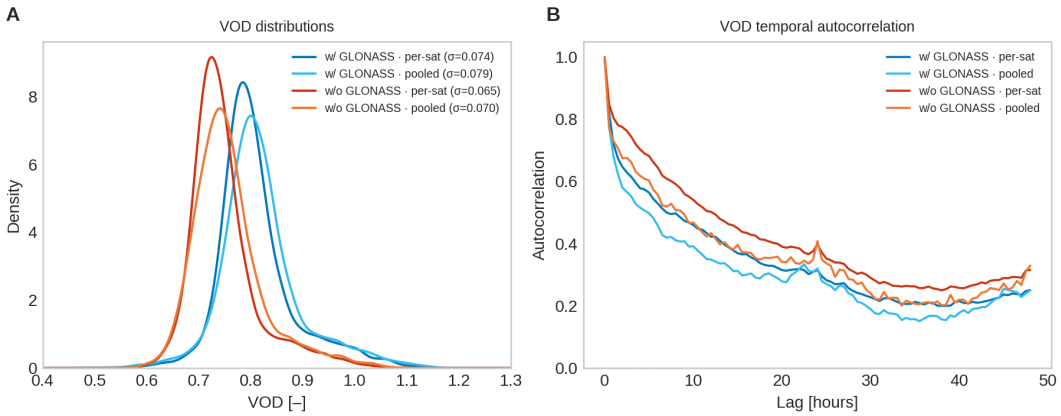


Figure S3: Comparison of the quality of GNSS-T VOD time series products calculated for including or excluding data from the GLONASS system, and by using the baseline anomaly algorithm proposed by [3] (where GLONASS and non-GLONASS systems are separate sets for the sky-sector-wise average) or satellite-wise calculations of the anomalies. The latter take the individual attenuation properties of each satellite into account. a) Distribution of 30-min VOD data, b) temporal autocorrelation. We find that removing GLONASS and choosing per-satellite anomaly calculation yields the lowest standard deviation (σ=0.065), hence, a more effective noise reduction. Simultaneously, this option shows the highest autocorrelation, indicating less correlation with noise on short time scales. The density peak of the per-satellite product also sits at a slightly lower VOD, since a mean pooled over all satellites is likely more strongly influenced by individual high-VOD satellites, whereas the per-satellite calculation weights every satellite equally. Tharandt; DOY 116–366. Only incidence angles $< 60°$ are shown.

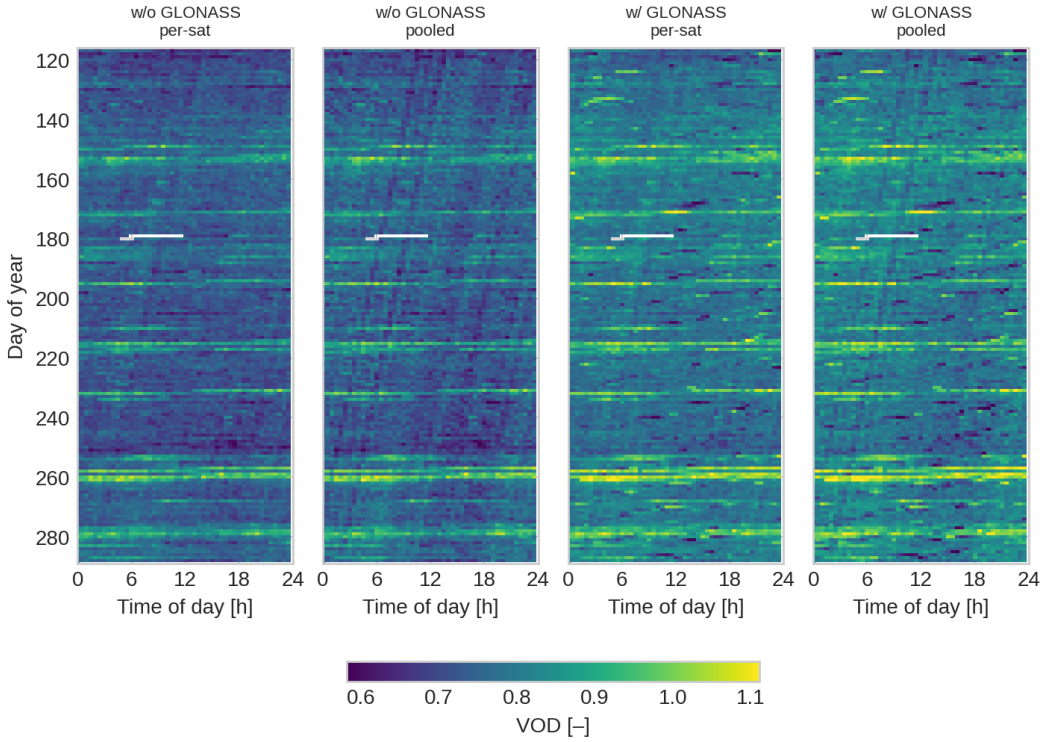


Figure S4: Temporal evolution of the GNSS-T VOD diurnal cycle. Please refer to fig. S3 for detailed description of the subplots. We observe diagonal aliases in all time series, likely orbit pattern induced that probe different parts of the inhomogeneous canopy. Excluding GLONASS and introducing satellite-wise anomaly calculation as an extension to the algorithm presented by [3] yielded a time series with least artifacts as in sudden jumps and alleviation of the aliases. Tharandt; DOY 116–366. Only incidence angles $< 60°$ are shown.

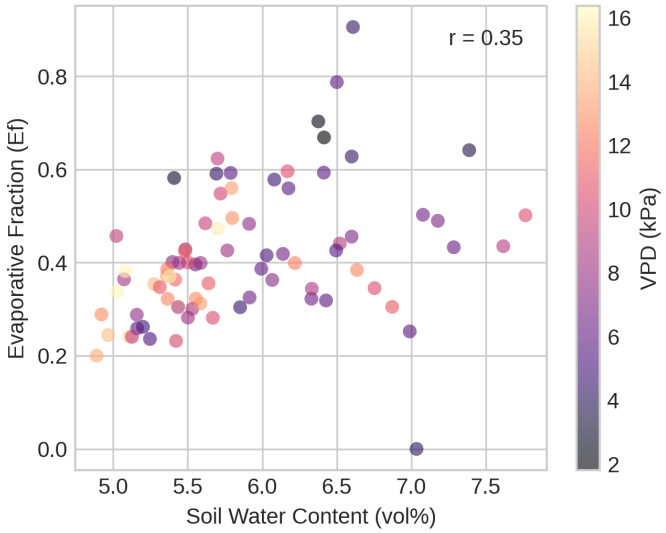


Figure S5: Indication for energy or not water limitation in the Tharandt ecosystem in 2024. The evaporative fraction (Ef=LE/Rn, latent heat flux/net Radiation) is the fraction of energy used for evaporation from all available energy. For a water limited ecosystem, a positive slope between critical soil water content and to soil wilting point is proposed while well-watered conditions show a constant ratio. We infer the inflection point between the two state at 5.5 vol% soil water content, $\mathrm{SWC}_{\mathrm{crit}}$.

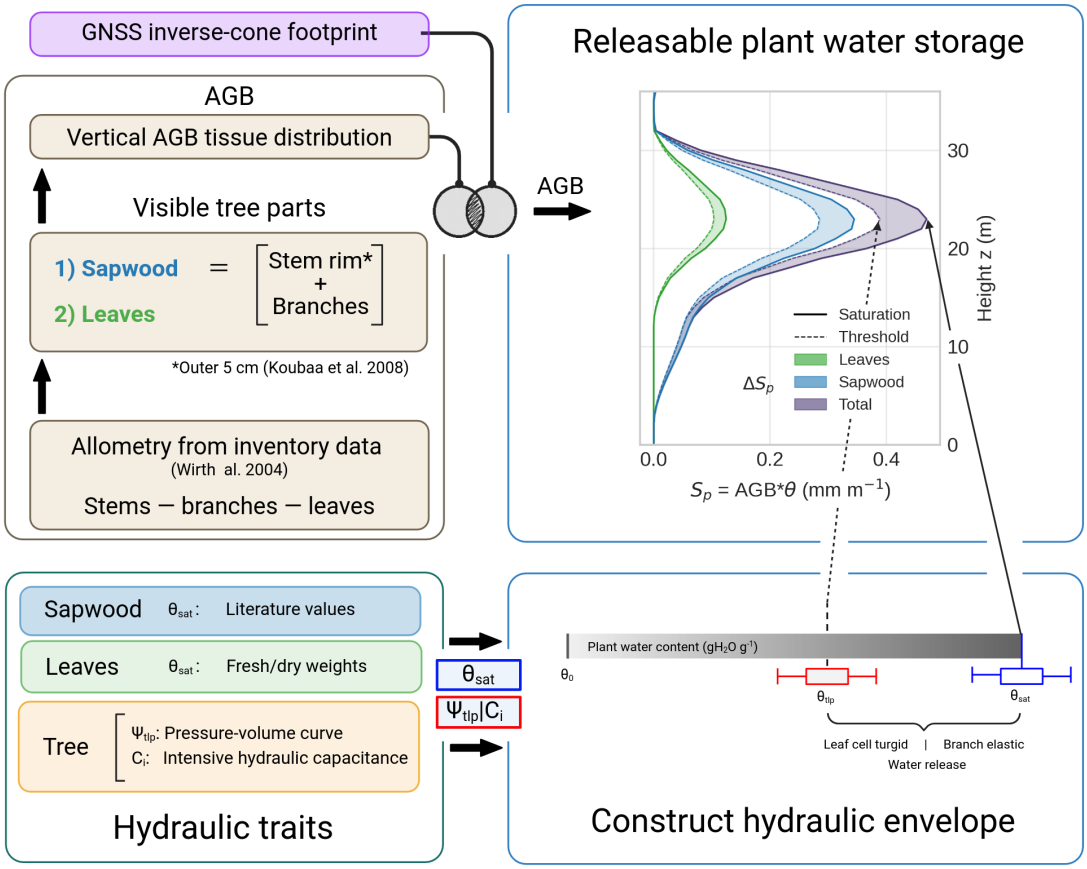


Figure S6: Workflow to calculate the maximum releasable water storage $\Delta S_p^{\max}$ from inventory data of AGB, the GNSS cone footprint, and hydraulic traits.

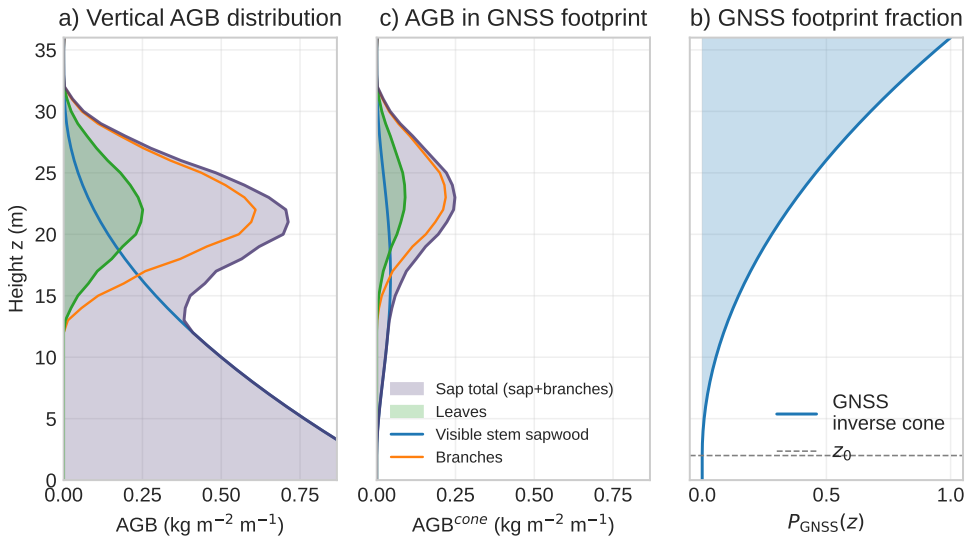


Figure S7: a) Above-ground biomass (AGB) of sapwood and leaves. Sapwood is the sum of branches, which are assumed to be entirely sapwood, and visible sapwood of the stem (top 2 cm). b) AGB falling into GNSS footprint. c) Fraction of canopy falling into GNSS footprint.

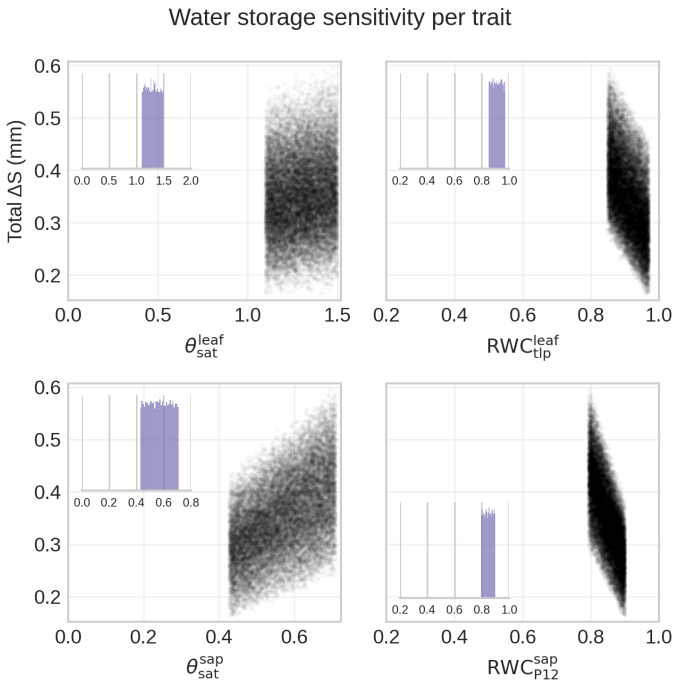


Figure S8: Monte-Carlo simulations of hydraulic traits and their effect on maximum releasable water storage ΔS_p for leaves and sapwood. We drew 20,000 random samples from an uniform trait distribution confined by the report ranges in tab. The inlet displays the prior distributions.

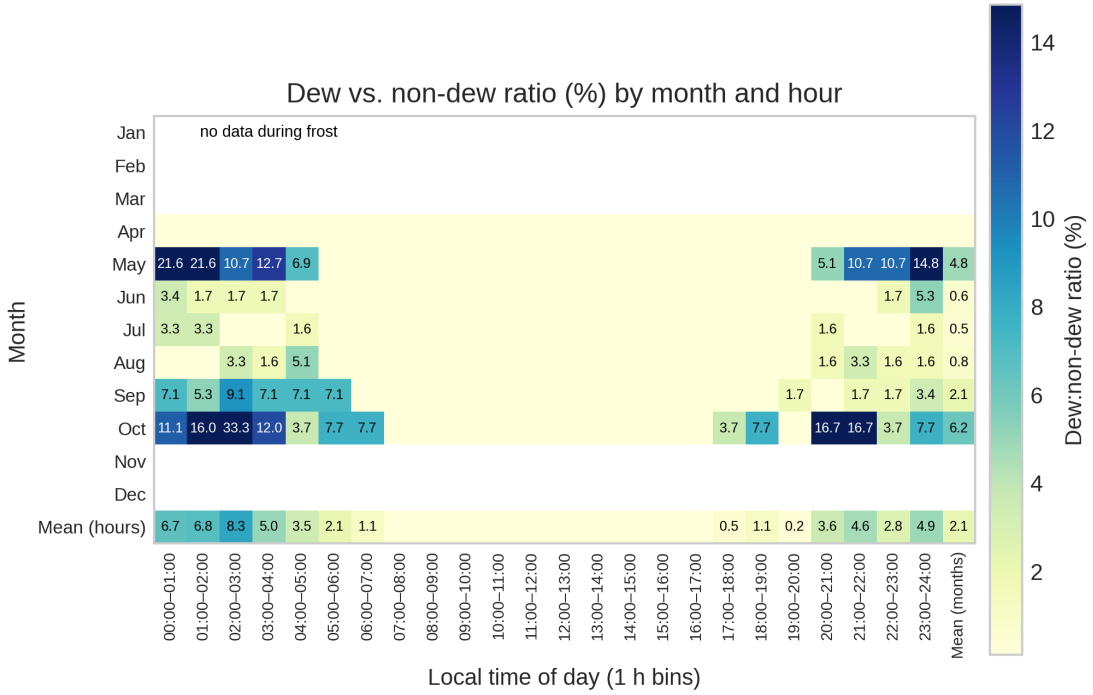


Figure S9: Dew occurrence defined by hydrometeorolgical filters at Tharandt

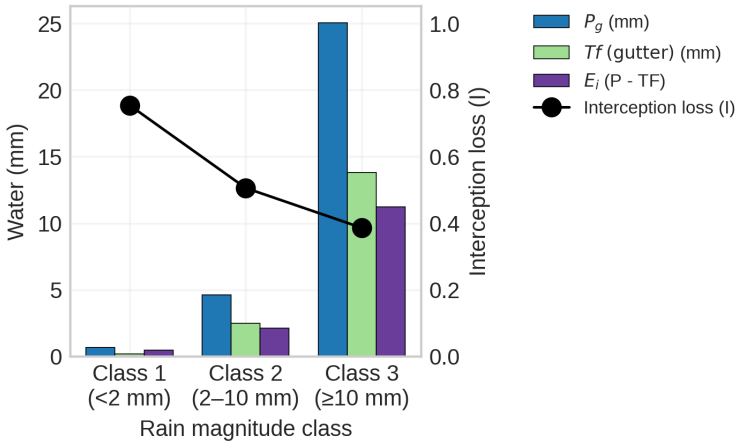


Figure S10: Interception loss per rainfall event class. Canopy influx is given as gross precipitation P_g, effluxes are measured throughfall Tf from the collection gutter and calculated evaporation from interception from the mass balance $E_i = P_g - Tf$.

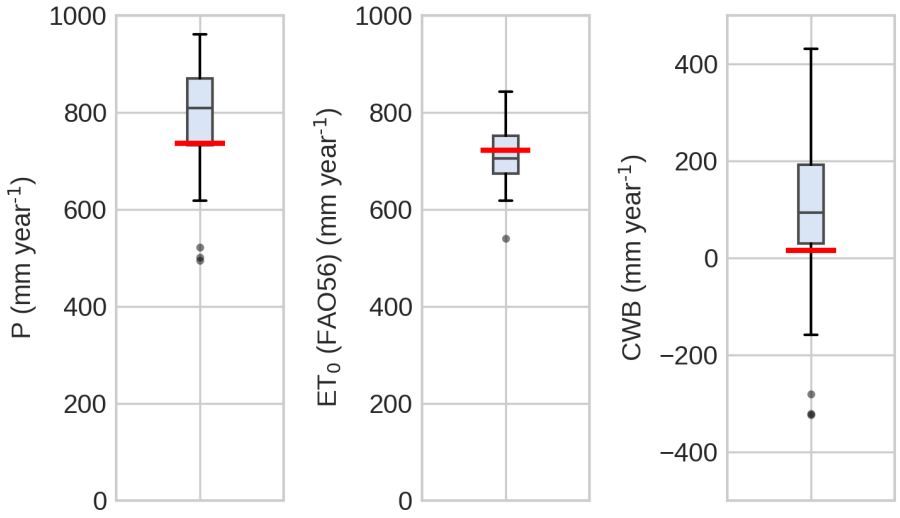


Figure S11: Comparing the climatic water balance (CWB, right) of the study period 2024 (marked in red) with the climatology of the preceding year (1995-2023) at Tharandt. Precipitation (left), potential evapotranspiration (middle, after FAO penmen-monteith equation for a plain grass surface [1], and CWB=P-ET_0. 2024 is at the 24th percentile of CWB.

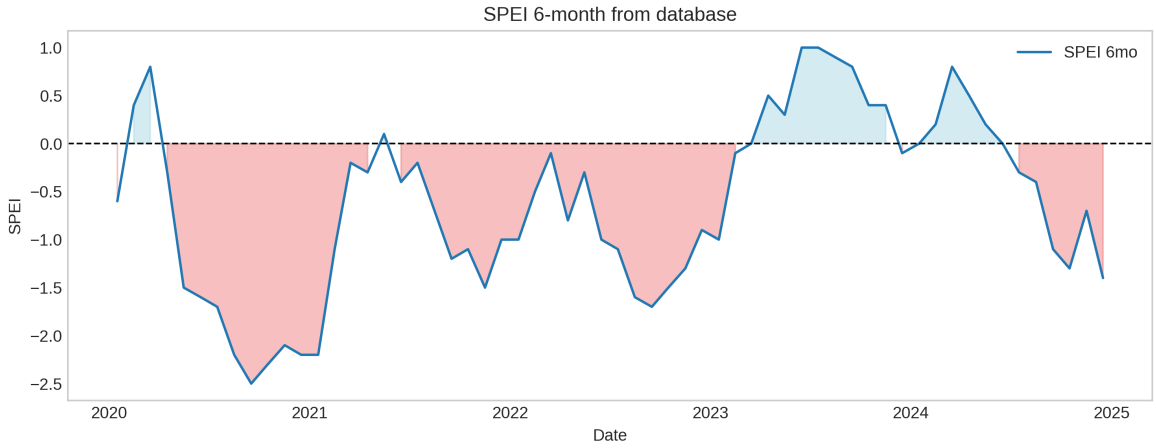


Figure S12: Standardized Precipitation Evapotranspiration Index (SPEI) with 6-month baseline of Niwot Ridge Forest research stie (US-NR1). The study period of [2] was 2022 and 2023.

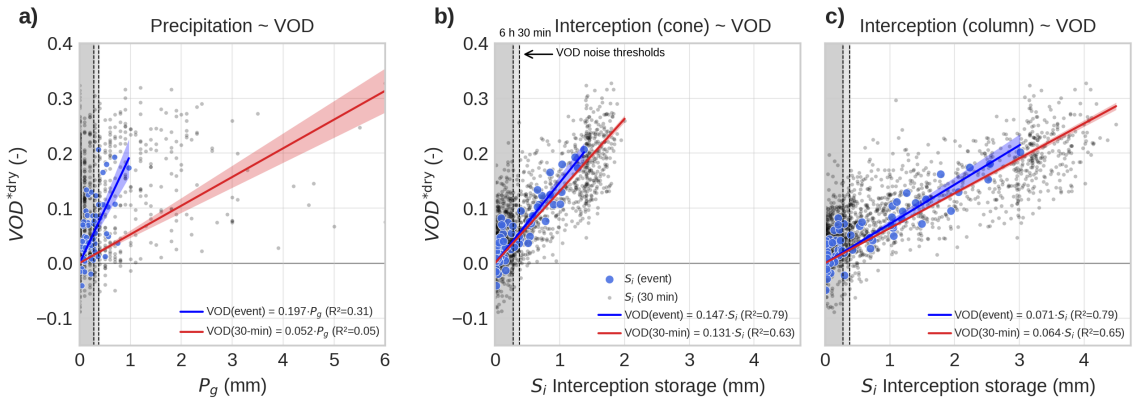


Figure S13: As Fig. 4 of the main text, but with confidence bands derived from the sampling error of the slope alone, i.e. without the calibration uncertainty of the *CanWat* storage. Shown for comparability with the preprint version of this study.

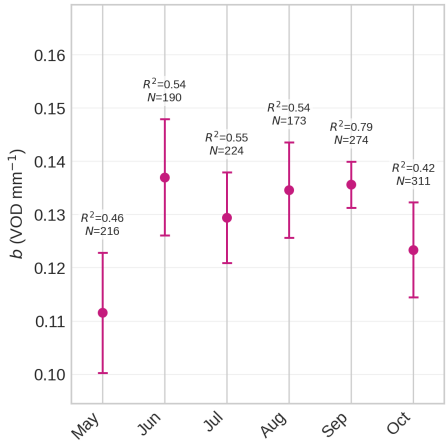


Figure S14: As Fig. 5 of the main text, but with confidence intervals derived from the sampling error of the slope alone. The month-to-month contrasts are resolved here because the *CanWat* calibration term, which is common to all months, is excluded.

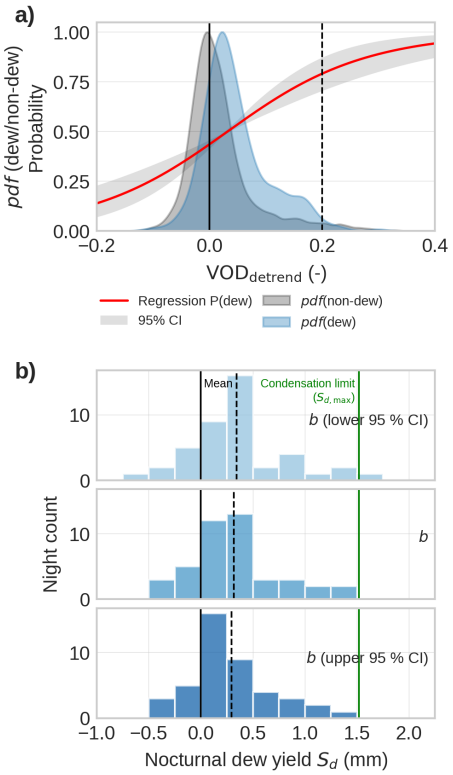


Figure S15: As Fig. 7 of the main text, but with the dew yield evaluated at the ends of the confidence interval of the monthly slope that excludes the *CanWat* calibration term.

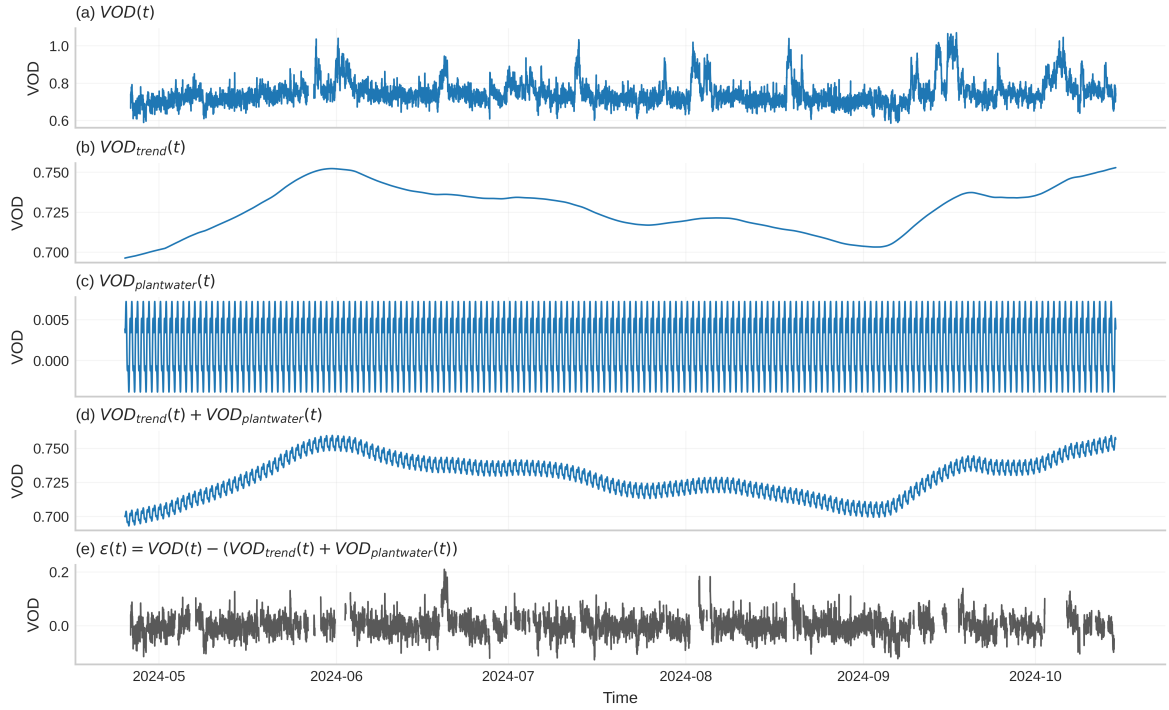


Figure S16: Decomposition of the GNSS-T VOD time series used to isolate the noise term $\epsilon(t)$: (a) the normalized VOD series; (b) the 14-day centered running median $\mathrm{VOD}_{\mathrm{trend}}(t)$; (c) the stationary diurnal Fourier series $\mathrm{VOD}_{\mathrm{plantwater}}(t)$ at harmonic order $k = 3$; (d) the sum of both deterministic components; and (e) the residual $\epsilon(t)$. Periods with dew or interception are masked before the decomposition. Note the differing vertical scales. The diurnal component has an amplitude of the order of 0.01, well below the residual scatter in (e).

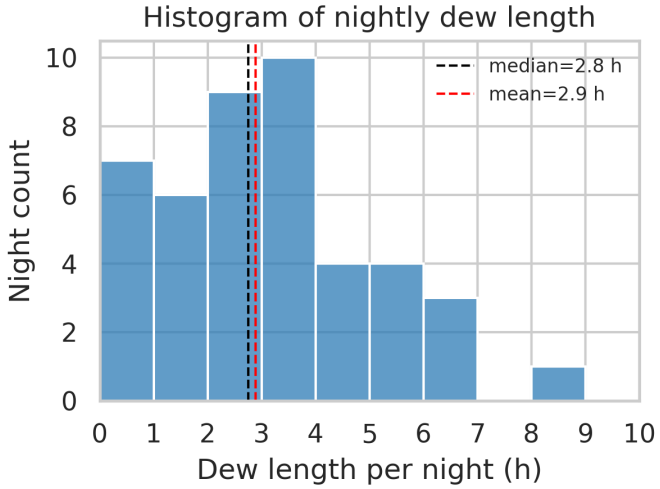


Figure S17: Histogram of the nightly dew duration over the study period, derived from the hydrometeorological filter set defined in Sect. 2.5 of the main text. Dew length varies strongly between nights, with a median of 2.8 h and a mean of 2.9 h; only few nights reach or exceed 6 h.

Table S1: Regression results of VOD on interception storage S_i at 30-min and event-scale aggregation for the season-wide fit of b for two spatial subsets: the inverted cone shape (the real GNSS look geometry), and a respective column (used for analysis per ground-area). Here, the confidence interval (CI) and the standard error (SE) of b contain the OLS sampling error alone, i.e. the uncertainty of the *CanWat* model is not propagated. These margins only state how precisely the regression line is determined by the data and are therefore considerably narrower than those in the main text.

GNSS footprint	Scale (N)	b [95 % CI] (VOD mm^{-1})	SE(b) (VOD mm^{-1})	R^2
cone	30 min (1388)	0.131 [0.128, 0.134]	0.002 (1.2 %)	0.634
	event (69)	0.149 [0.137, 0.162]	0.006 (4.2 %)	0.807
column	30 min (1611)	0.064 [0.062, 0.065]	0.001 (1.2 %)	0.654
	event (69)	0.073 [0.066, 0.079]	0.003 (4.6 %)	0.797

Table S2: Same as Table S1, but for the monthly fits of b , and only for the cone geometry. Both the OLS-only and the OLS + *CanWat* 95 % confidence intervals are given.

Window	b (VOD mm^{-1})	95 % CI (VOD mm^{-1})		RMSE	R^2	N
		OLS + *CanWat*	OLS only			
May 2024	0.112	[0.058, 0.165]	[0.100, 0.123]	0.049	0.46	216
Jun 2024	0.137	[0.072, 0.202]	[0.126, 0.148]	0.048	0.54	190
Jul 2024	0.129	[0.068, 0.191]	[0.121, 0.138]	0.049	0.55	224
Aug 2024	0.135	[0.071, 0.199]	[0.126, 0.144]	0.063	0.54	173
Sep 2024	0.136	[0.072, 0.200]	[0.131, 0.140]	0.043	0.79	274
Oct 2024	0.123	[0.065, 0.182]	[0.114, 0.132]	0.052	0.42	311

References

[1] Allen, R.G., Pruitt, W.O., Wright, J.L., Howell, T.A., Ventura, F., Snyder, R., Itenfisu, D., Steduto, P., Berengena, J., Yrisarry, J.B., Smith, M., Pereira, L.S., Raes, D., Perrier, A., Alves, I., Walter, I., Elliott, R., 2006. A recommendation on standardized surface resistance for hourly calculation of reference ETo by the FAO56 Penman-Monteith method. Agricultural Water Management 81, 1–22. URL: https://www.sciencedirect.com/science/article/pii/S037837740500154X, doi:10.1016/j.agwat.2005.03.007.

[2] Burns, S.P., Humphrey, V., Gutmann, E.D., Raleigh, M.S., Bowling, D.R., Blanken, P.D., 2025. Using GNSS-based vegetation optical depth, tree sway motion, and eddy-covariance to examine evaporation of canopy-intercepted rainfall in a subalpine forest. EGUsphere , 1–38URL: https://egusphere.copernicus.org/preprints/2025/egusphere-2025-1755/, doi:10.5194/egusphere-2025-1755. publisher: Copernicus GmbH.

[3] Humphrey, V., Frankenberg, C., 2023. Continuous ground monitoring of vegetation optical depth and water content with GPS signals. Biogeosciences 20, 1789–1811. URL: https://bg.copernicus.org/articles/20/1789/2023/, doi:10.5194/bg-20-1789-2023.